Well-defined sub-nanometer graphene ribbons synthesized inside carbon nanotubes

Well-defined sub-nanometer graphene ribbons synthesized inside carbon nanotubes

Hans Kuzmany[2*], Lei Shi[1,2*] Sofie Cambré[3], Miles Martinati[3], Wim Wenseleers[3], Jenő Kürti[4], János Koltai[4], Gergő Kukuczka[4], Kecheng Cao[5], Ute Kaiser[5], Takeshi Saito[6], & Thomas Pichler[2]

[1]*School of Materials Science and Engineering, State Key Laboratory of Optoelectronic Materials and Technologies, Nanotechnology Research Center, Sun Yat-sen University, Guangzhou 510275, Guangdong, P. R. China*

[2]*Faculty of Physics, University of Vienna, 1090 Wien, Austria*

[3]*Experimental Condensed Matter Physics Laboratory, Physics Department, University of Antwerp, B-2610 Antwerp, Belgium*

[4]*Department of Biological Physics, ELTE Eötvös Loránd University, Pázmány Péter stny. 1/A, 1117 Budapest, Hungary*

[5]*Central Facility for Electron Microscopy, Electron Microscopy Group of Materials Science, Ulm University, Ulm 89081, Germany*

[6]*Nanotube Research Centre, National Institute of Advanced Industrial Science and Technology (AIST), 305-8565 Tsukuba, Japan*

Graphene nanoribbons with sub-nanometer widths are extremely interesting for nanoscale electronics and devices as they combine the unusual transport properties of graphene with the opening of a band gap due to quantum confinement in the lateral dimension. Strong research efforts are presently paid to grow such nanoribbons. Here we show the synthesis of 6- and 7-armchair graphene nanoribbons, with widths of 0.61 and 0.74 nm, and excitonic gaps of 1.83 and 2.18 eV, by high-temperature vacuum annealing of ferrocene molecules inside single-walled carbon nanotubes. The growth of the so-obtained graphene nanoribbons is evidenced from atomic resolution electron microscopy, while their well-defined structure is identified by a combination of an extensive wavelength-dependent Raman scattering characterization and quantum-chemical calculations. These findings enable a facile and scalable approach leading to the controlled growth and detailed analysis of well-defined sub-nanometer graphene nanoribbons.

1 Keywords

graphene nanoribbons, electronic structure, Raman scattering, resonance profiles, Albrecht theory, GW calculation

2 Introduction

Sub-nanometer graphene ribbons (graphene nanoribbons, GNRs) are promising structures for future electronic devices[1,2] as they are considered of unifying the unique electronic properties of graphene [3] with a reasonably sized gap in their electronic structure. The gap results from quantum confinement in the lateral direction and consequently scales with the inverse width of the ribbons. [4,5] The ribbons are strips of carbon atoms cut out from a graphene lattice. At present most common strips are of the armchair type, i.e., the edge of the ribbons consists of coaxial carbon pairs oriented parallel to the direction of the ribbon axis (armchair graphene nanoribbons (AGNR)). They are characterized by the number n of such pairs across their width. The electronic structures of AGNR can be classified into n= 3p, 3p+1 and 3p+2 species, where p is an integer.[4] One of the most commonly investigated structures is the n=7 AGNR (7-AGNR) [6,7] with band gaps between 2.1 and 2.3 eV as reported from scanning tunneling spectroscopy (STS) and optical studies. [8] More recently ribbons with more complex topologies were grown which have coved zigzag, chevron or chiral type structures.[7,9,10] The ribbons are usually grown on Au substrates from preselected and properly designed flat poly-aromatic hydrocarbon molecules (PAHs).[11] In this case the PAHs are vacuum deposited on the substrate and subsequently transformed to polymeric units with nanoribbon structure. To take advantage of the ribbons grown in this way subsequent transformation to insulating substrates is necessary. [12] Raman scattering was used to evidence that the nanoribbons do not suffer in quality by this transformation.

In general the carbons at the edge of the ribbons are saturated by hydrogen but by selecting

special PAHs, bandgap engineering [13–15], construction of ribbon heterojunctions [16,17] and ribbons with unusual electronic properties[18] have been demonstrated where topological properties of the ribbons under investigation play an important role. Most recently ribbons became relevant for applications in photocatalytic hydrogen generation.[19]

Besides STS and electron microscopy, Raman scattering has repeatedly been used to characterize GNR. Several Raman active vibrational modes were identified to characterize the ribbons. Such modes are among others the radial breathing like mode (RBLM), the CH in plane bending mode (CH-ipb), the D line, and the graphene G line.[12,13] The RBLM frequency scales with (the square root of) the inverse ribbon width,[20,21] and is the pendant to the radial breathing mode of the carbon nanotubes.

Filling and consecutive chemical reactions inside single-walled carbon nanotubes (SWCNTs) is a promising technique to grow new nanoscale materials in general.[22–24] In addition, the one-dimensional geometry of the CNTs is an excellent template for the controlled growth of conventional or exotic low-dimensional compounds.[25–27]. Here, we show that this in-tube synthesis can be used to grow GNRs with well-defined sub-nanometer width. Growth of such narrow ribbons with controlled width has previously been limited to the polymerization of specific PAHs on Au substrates.[28] Although providing well-defined freestanding ribbons with relatively high yield, the flexibility of preparing GNRs with different widths and structures is limited by the availability of appropriate precursor molecules. When synthesizing GNRs inside SWCNTs, the width of the GNRs is determined by the diameter of the SWCNTs, hence could in the future be flexibly

tuned by starting from CNT samples with different diameters (eventually even diameter/chirality-sorted SWCNTs). Moreover, the hybrid structures of encapsulated ribbons and a semiconducting SWCNT, both with a different band gap can be interesting also from a materials design perspective.

The growth of GNRs inside SWCNTs has been demonstrated by first filling the SWCNTs with flat precursor molecules, such as coronene[29,30] or other PAHs[28], and subsequently transforming them at elevated temperature. Although these initial results were very promising, growth of high-quality specific types of GNRs with well-defined widths still remained a challenge. In particular the analysis of the electronic properties of the objects inside the tubes remained difficult due to the overlapping electronic transitions of the carbon nanotubes themselves. To avoid this overlap, functionalization was necessary of the otherwise pristine tubes.[31] As it will be demonstrated below, Raman scattering, in particular in combination with evaluation of resonance Raman excitation profiles, is an excellent tool to reveal the electronic structure of the objects inside the tubes. This is due to the double selective nature of the resonance Raman scattering process. It is selective with respect to the geometrical structure of the objects by the vibrational mode but also selective with respect to the electronic structure by the resonance profile. Small width of the Raman lines indicates well-defined geometrical structures and sharp excitation profiles provide evidence for uniform electronic configuration of the GNRs.

In this work, we demonstrate the synthesis of two specific GNRs, i.e., 6- and 7-AGNRs, with well-defined geometrical structure, from the bulky molecule ferrocene ($FeCp_2$). Evidence for the growth of the AGNRs inside the tubes comes from aberration-corrected high-resolution

transmission electron microscopy (AC-HRTEM) and from Raman scattering. We also show that wavelength-dependent Raman spectroscopy gives direct access to the electronic and optical properties of the encapsulated objects by the evaluation of resonance Raman excitation profiles. This allows determining experimentally the excitonic gap and even more the electronic structure beyond the gap. High level first principle calculations provide for the first-time relative intensities of the Raman lines of the GNRs by using the Placzek formulation with energy dependent polarizabilities.[32] The latter procedure is a fundamental progress in the evaluation of Raman intensities.

3 Experimental Results and Analysis

Aberration-Corrected High Resolution Transmission Electron Microscopy (AC-HRTEM) The standard feature for the observation of encapsulated ribbons in TEM is an alternating pattern of narrow and wide signals from the material inside.[28,33] It originates from an electron beam induced twisting of parts of the ribbons. Figure 1 depicts a collection of results from $FeCp_2$ filled and subsequently transformed SWCNT species as acquired by the SALVE instrument with Cs/Cc aberration corrector. It demonstrates the twisting of the graphene ribbons by the electron beam (panel a-e) and provides images of the ribbons in atomic resolution with corresponding simulations (panel f-j). The time-dependent AC-HRTEM images show clearly that the observed species are flat objects, that twist under the influence of the electron beam, and cannot be identified as inner nanotubes. The AC-HRTEM images (panels f-j) provide clear evidence of the atomic structure of the ribbons, however, also demonstrate that the nanoribbons are very unstable under

the electron beam and defects along the length of the structure are quickly generated by the beam. Therefore, these AC-HRTEM images are not representative for the quality of the as-grown ribbons and only serve to evidence that the structures are flat ribbons. Evidence for the well-defined electronic structure of the as-grown ribbons comes from our detailed wavelength-dependent Raman spectroscopic experiments (see below). More details on the AC-HRTEM are provided in the Supporting Information Section (a).

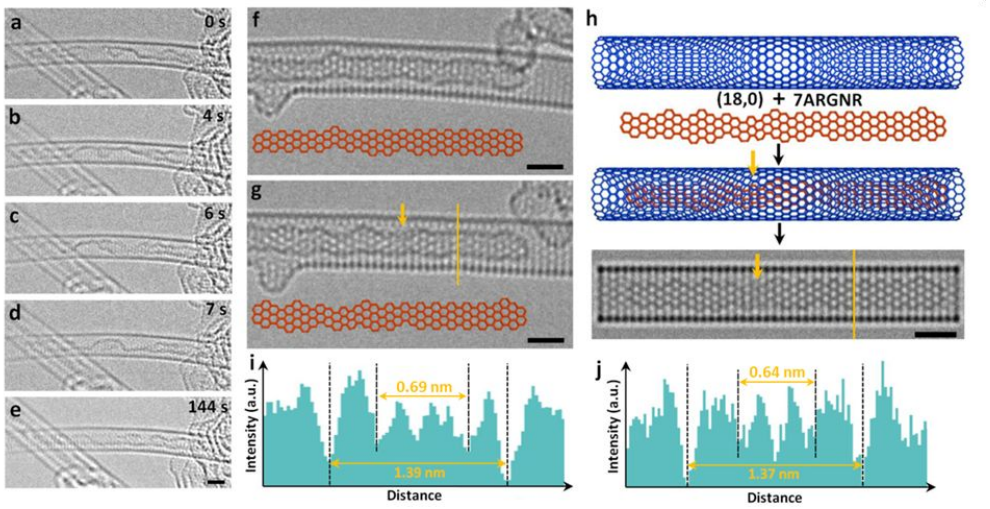

Figure 1: AC-HRTEM images and corresponding simulations for AGNR@SWCNTs. a-e, Time series of images showing a ribbon confined in a SWCNT twisting under 80 keV electron beam. The modulation of the response with time is evidence for a flat ribbon. f,g, Two typical AC-HRTEM images in atomic resolution showing a flat 7-AGNR dominated structure confined in a SWNT. Scale bar is 1 nm. The inserted models in red present the corresponding structure of the ribbon, showing also the instability of the ribbon under electron beam irradiation (i.e., f-g are the same ribbon but acquired after different exposure times). h, TEM image simulation for confirming the structure of 7-AGNR@SWCNT in g. It depicts the tube (18,0), the ribbon, the combination of the two and the simulation. The most part of 7-AGNR and the wall of SWNT are AA stacked showing clear graphene structure for the former, while a small mismatch part as indicated by yellow arrows results in blurred contrast in the simulated TEM and in the raw TEM image in g. i,j, Intensity profiles along the yellow line of the recorded pattern i and of the simulated pattern j. The round (outer) tubes exhibit a strong reduction of contrast at the edge whereas the contrast is weaker at the edge of the flat ribbons. Indicated distances correlate with the diameter of a (18,0) tube and evidence a net ribbon width between 0.64 and 0.69 nm.

Raman Scattering Previously, we reported the observation of a set of Raman lines after thermal conversion of $FeCp_2$ filled SWCNT [24,34] but the origin of these lines remained unclear as they did not fit to proper model calculations and high resolution TEM was not available. Here we identified the origin of the Raman lines which turned out to be very sensitive to transformation temperature. Figure 2a-d depicts this behavior in a plot where Raman intensities are characterized by a color code as a function of Raman frequency and transformation temperature. Raman spectra were normalized to the 2D band which is least influenced by the changes induced by the GNR encapsulation. Figure 2a,b depicts the responses measured for 568 nm excitation while Fig. 2c,d presents those for 633 nm excitation. At low temperature, only the RBMs (around 200 cm^{-1}) and the G-line of the SWCNTs (around 1600 cm^{-1}) are observed. When increasing the transformation temperature beyond 500 °C, depending on the excitation laser used two groups of Raman lines can be observed. They exhibit a maximum Raman intensity between 600 and 700 °C, indicated by the horizontal white arrows in the figure. As shown further on, these two groups of lines correspond to the in-tube synthesis of AGNRs with different widths.

The lower panels of Fig. 2 depict the Raman spectra explicitly. Panels e and f are spectra recorded at 568 nm (transformation temperature 600 °C) and g and h are spectra recorded at 633 nm (transformation temperature 700 °C), for two different Raman frequency regions. When comparing the Raman spectra of the ferrocene-filled and temperature-transformed samples (red) with the spectra of filled SWCNTs without transformation (black), the new Raman features appear very well separated from the response of the SWCNTs in general. In the high-frequency region, the spectra of the SWCNTs can be subtracted straight forwardly, yielding the Raman response

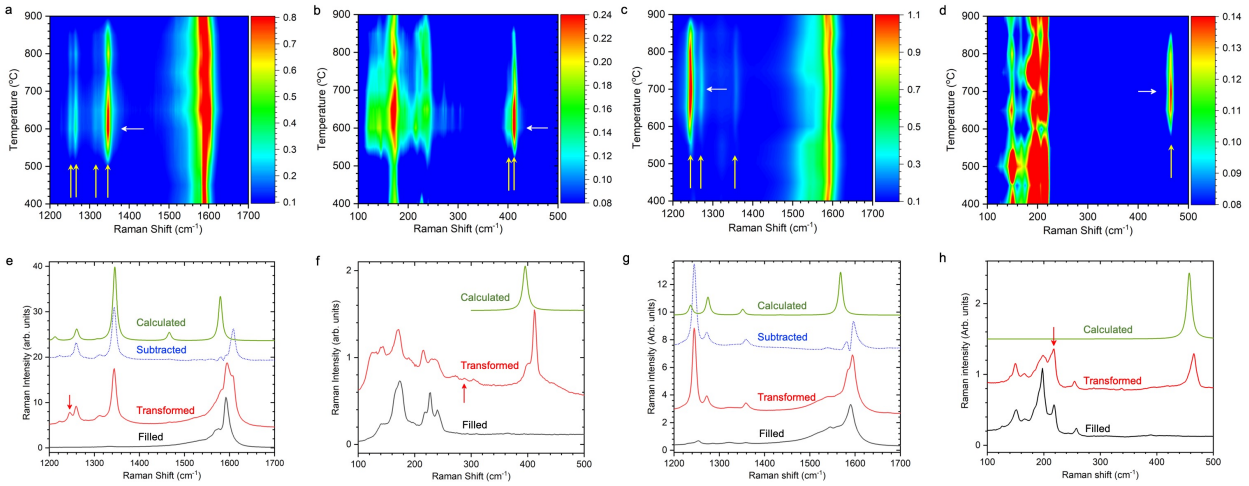

Figure 2: Raman scattering for temperature dependent transformation. a-d, Color-code maps for Raman line intensities observed after transformation of $FeCp_2$@SWCNTs as a function of Raman frequency and transformation temperature. The latter was increased in 50 °C steps. Vertical white arrows highlight the positions of the main new Raman lines. Horizontal white arrows are located at temperatures of maximum Raman response. Raman spectra in a and b and in c and d were excited with a yellow laser (568 nm) and red laser (633 nm), respectively. e-h, Raman spectra for $FeCp_2$@SWCNT tuned by transformation temperature to optimized response for the two groups of lines. e, Spectra as observed for yellow laser excitation at 568 nm in the high frequency region, from bottom to top: tubes filled with $FeCp_2$ (black) and subsequent transformation at 600 ∘C (red), AGNR contribution by subtracting the Raman signals from the nanotubes (blue, dotted), and calculation (green) for 7-AGNR. The Raman line marked by a down-arrow was also subtracted since it originates form 6-AGNR as discussed below. f, Raman signals from low frequency region, from bottom to top: filled tubes, transformed at 600 °C, and calculated for 7-AGNR. The arrow marks the response from DWCNTs obtained during the transformation process. g,h, Similar spectra as in e,f but for transformation temperatures of 700 °C, recorded with 633 nm laser, and as calculated for 6-AGNR.

of the newly synthesized objects (blue dotted spectra in panels e and g). For the low-frequency region, a subtraction is more difficult, since during the transformation also inner tubes are formed thereby changing the response of the SWCNTs as well (red arrows). Even though, due to their higher frequency, the lines from the RBLMs of the GNRs can be well separated from the response of the CNTs. The figures demonstrate very narrow line widths of the order of 10 cm^{-1} for the response of the nanoribbons. This linewidth is equivalent to the Raman response of high-quality ribbons grown on Au substrates and subsequently transferred to semiconducting substrates.[2,12,35] Such narrow line widths (in combination with a clear resonance profile) can only be observed for nanoribbons with a well-defined width along the entire length, as width variations would lead to inhomogeneous broadening of the lines or even disappearance of the RBLM mode. Figure 2 also presents the calculated Raman spectra for 7-AGNR species (panels e and f, in green) and for 6-AGNR (panels g and h, in green), which were obtained from first principle calculations using the dynamical Placzek formalism [32]. More details about these calculations are in the Method section and in the Supporting Information Sections (b). They correspond very well to the observed experimental lines, even in relative intensity. A blown up version of this comparison can be found in the Supporting Information Section (d). For the 7-AGNR, the high-frequency modes are accordingly identified as the CH-ipb mode (1258 cm^{-1}), the D-line (1344 cm^{-1}) and the G line (1606 cm^{-1}). The low frequency mode at 414 cm^{-1} (with small shoulder at 400 cm^{-1}) can be identified as the RBLM. Likewise, for the 6-AGNR the RBLM is located at 465 cm^{-1}, the CH-ipb mode at 1243 cm^{-1}, the D-line at 1358 cm^{-1} and the G line at 1595 cm^{-1}. Note that the latter is strongly overlapping with the G line of the SWCNTs which prevents its direct determination from

the difference (blue) spectra. However, the frequency can be obtained by measuring the sum of the CH-ipb and the G line of the ribbons which is observed at 2839 cm^{-1}. This localizes the G line at 1595 cm^{-1}.

Table 1 presents the experimental Raman frequencies and line widths for both the 6-AGNR and 7-AGNR and compares it to our theoretical values as well as to values for the same modes measured on Au-substrates for 7-AGNR.[6] For the 6-AGNR a comparison is made with the only reported data originating from the fusion of linear chains of poly-paraphyenlye at 800 K.[36] The agreement between calculated and experimentally determined Raman frequencies in the high-frequency region is better than 2% and also the agreement between calculated and experimental relative line intensities is excellent, except for the CH-ipb of the 6-AGNR which appears too weak in the calculation. The table highlights the unusually narrow width of the Raman lines from the encapsulated species. In three very recent reports, Raman spectra for 7-AGNR grown on Au substrates and subsequently transferred to transparent substrates are shown to exhibit similar narrow line widths as observed here.[2,12,35]

Raman Excitation Profiles Raman excitation profiles were measured for all Raman lines in the low and in the high frequency region for the excitation wavelength range from 400 - 800 nm with 5 nm steps. Figure 3a shows overall results in the form of a two-dimensional Raman map for a sample transformed at a temperature of 850 °C. Raman map means Raman intensities are plotted on a color code versus Raman shift and excitation energy. The procedure to create the Raman map from the experiments and to extract the excitation profiles for the various modes by wavelength-

Table 1: Raman lines of 7-AGNR and 6-AGNR; Frequencies (ω_{ph}), intensities (weak (w), medium (m), strong (s), very strong (vs)), and linewidths W (FWHM, in parentheses) for the observed Raman lines (column Exp.) as compared to calculation (column Calc.) and to reference (column Ref.). For 7-AGNR and 6-AGNR the latter are from reference[6] and reference[36], respectively. The column with the calculated frequencies depicts also the difference to the experiment in %. The last two columns depict the excited state frequencies (ω^*_{ph}) and the Huang-Rhys factor (HR) for the first excited state, both obtained from a fit of the resonances to the Albrecht A-term. All frequencies are given in cm^{-1} and rounded to integer values.

Mode	ω_{ph} (W) Exp. (cm^{-1})	ω_{ph} Calc.;% (cm^{-1})	ω_{ph} (W) Ref.[6,36] (cm^{-1})	$\omega_{ph}{}^*$ from fit (cm^{-1})	HR from fit (cm^{-1})
7-AGNR					
RBLM	414m (7.5)	395m; 4.5	395m (22.1)	434	0.08
CH-ipb	1258s (9.6)	1261s; 0.2	1263s (30)	1195	0.25
D	1342vs (10.8)	1345vs; 0.2	1344vs (26)	1275	0.25
G	1607s (13)	1580 s; 1.7	1607vs (31)	no fit	
6-AGNR					
RBLM	466m (8)	457m; 1.7	not reported		
CH-ipb	1243vs (9.6)	1236m; 0.6	1245s (100)	1281	0.17
	1272m (10.6)	1272s; 0		1272	0.25
D	1358m (11.4)	1352w; 0.4	1315m	1358	0.25
G	1595	1568s; 1.7	1590vs[13]	no fit	

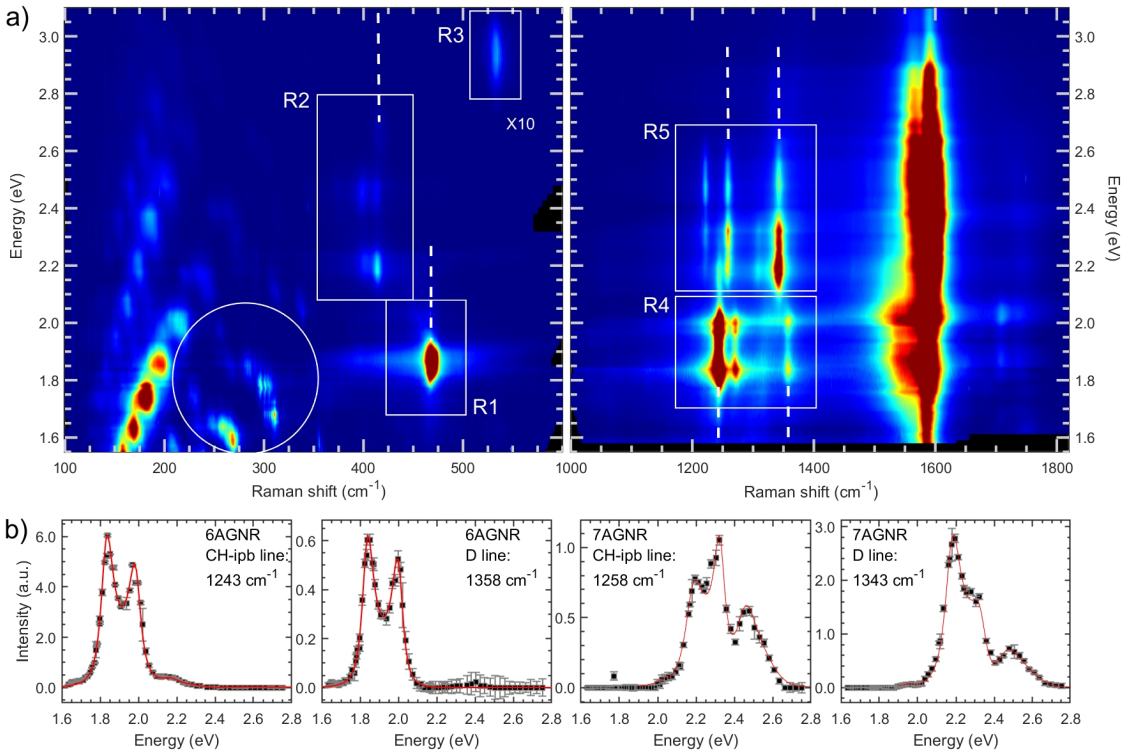

Figure 3: Wavelength-dependent Raman spectroscopy of AGNR@SWCNT. a, Two-dimensional Raman map for the resonance excitation of AGNR@SWCNT. The features from the ribbons are framed into the white rectangles with numbers R1 to R5. The rectangles R2 and R5 correspond to the 7-AGNR whereas rectangles R1 and R4 correspond to the 6-AGNR. R3 (intensity multiplied by 10) most likely originates from 5-AGNR (see below). The bulky feature around 1600 cm^{-1} comes mainly from a superposition of the the G line of the nanotubes and the AGNR. The circled signals originate from double-walled carbon nanotubes grown during transformation. They correspond to the weak Raman lines in Fig. 2e,f assigned by the arrows. b, Experimental Raman excitation profiles derived for the Raman peaks that are indicated by the dashed white lines in panel a are presented as black squares together with the fitted Raman excitation profiles (in red) for the 6-AGNR (left) and 7-AGNR (right) (See also Supporting Information section (e)). The profiles correspond to the CH-ipb and D-line, respectively.

dependent fitting of the experimental data, is described in detail in the Supporting Information Section (e). The features between 1.7 and 2.1 eV excitation in the lower part of the map (R1 and R4) correspond to the 6-AGNR. The upper part has the resonances of the 7-AGNR (R2 and R5). R3 is the resonance of a weak and as yet unknown new line to be discussed below.

For a selected number of modes such as the CH-ipb and the D line, experimental resonance profiles are plotted in Fig. 3b. The profiles for the 6-AGNR show only two vibronic peaks. In contrast, the resonances for 7-AGNR exhibit a highly structured profile which turned out to originate from vibronic sidebands as well as from higher exciton transitions.

The red lines in Fig. 3b are fits from the Kramers-Heisenberg-Dirac (KHD) theory for resonance Raman scattering [37,38] with wave functions in the adiabatic approximation. In this case the resonance scattering intensity I_s is given by

$$I_s = C I_0 \omega_s^4 \sum_{\rho\sigma} |(\alpha_{\rho\sigma})_{fi}|^2 \qquad \text{with} \tag{1}$$

$$(\alpha_{\rho\sigma})_{fi} = \sum_r \frac{\langle f|\mu_\rho|r\rangle\langle r|\mu_\sigma|i\rangle}{\omega_{ri} - \omega_L - \mathrm{i}\gamma_r}$$

where $I_0, (\alpha_{\rho\sigma})_{fi}, \mu_{\rho,\sigma}, \omega_{ri}$, and γ_r are the intensity of the incident light, the transition polarizability, the dipole moment, the transition energy from state i to state r, and an electronic damping constant, respectively. Within the adiabatic approximation for the wave functions and a transition dipole moment independent of the vibrational normal coordinates (Albrecht A-term [39]) this results eventually in the relation

$$(\alpha_{\rho\sigma})_{fi} = A = \sum_{e,\nu_e} \frac{\mu^e_{0\rho}\mu^e_{0\sigma}}{\omega_{ri} - \omega_L - \mathrm{i}\gamma_\mathrm{r}} \langle\nu_f|\nu_e\rangle\langle\nu_e|\nu_i\rangle \ . \tag{2}$$

$\mu^e_{0\rho,\sigma}$ are the ρ, σ components of the pure electronic transition dipole moments which are assumed to be constant. r stands as abbreviation for the transitions to states e, ν_e. The right part of the expression in Eq. 2 depicts the vibronic matrix elements given by the Frank-Condon (FC) integrals. The vibronic quantum numbers ν_i were assumed zero except for i=0. This means all electrons are in the vibronic ground state. ν_f was assumed 1 throughout meaning that only one vibron processes were considered. The experimental results for the 7-AGNR required electronic transitions up to $e = 2$, i.e., in solid state terminology E_{11} and E_{22} were needed for the fit and thus experimentally determined. The most relevant parameters for the fit are the transition energies to the first and to the second excited state, the Huang-Rhys factors, and the vibrational frequencies in these states. Values for the transition energies are depicted in Tab. 2. Excited state frequencies as they are listed in Tab. 1 were found to be very close to the ground state frequencies. For the resonance of the CH-ipb mode in the case of 7-AGNR the line width in the excited state for the transition E_{11} was considerably smaller than the line width in the ground state. Therefore the peak for the high energy resonance (outgoing resonance) is higher than the peak for the low energy resonance (incoming resonance). All parameters for the fitted resonances are summarized in the Supporting Information Section (f), Tab. S1. The observed transition energies were compared to values calculated by solving the Bethe-Salpeter equation within the frame of a quasiparticle self-consistent GW calculation. These calculations go beyond the energy dependent Placzek approximation as it was used to derive the Raman spectra described in Fig. 2. The calculation is described in detail in Methods and in Supporting Information Section (b). Table 2 lists the observed transition energies as compared to our calculations and to reported values from optical

reflection measurements [8]. The comparison depicted in the table further evidences the successful growth of 7-AGNR and 6-AGNR inside SWCNT.

The two peaks in the resonance for the 6-AGNR represent the transitions to the first and to the second vibronic level in the excited state, or equivalently, the ingoing and outgoing resonance. Higher vibronic levels are neither observed for the 6-AGNR nor for the 7-AGNR.

Calculated transition energies for 5-AGNR are included in the table since the values may be relevant for the resonance of the Raman line observed at 533 cm^{-1} (R3 in Fig. 3) as discussed below. The low value of 0.84 eV calculated for the band gap is consistent with the 3p+2 family of these ribbons.

For the analysis of AGNR@SWCNT the RBLMs are particularly important since they exhibit a strong and characteristic response in a frequency region which is free from other Raman lines. In the case of the 7-AGNR@SWCNT the response is unusual since it exhibits several components. Figure 4a shows a zoomed-in Raman map of region R2. Several peaks can be observed in this region, which become also evident when plotting the Raman spectra for two distinct laser excitations (Fig. 4b). The main peak (highest intensity) appears at a vibrational frequency of 414 cm^{-1} for 569.5 nm excitation with an exceptionally small line width of only 7 cm^{-1}. In addition, a shoulder can be observed around 400 cm^{-1}, which is considerably broader (13 cm^{-1}) and exhibits dispersion, i.e. line position shifts with changing excitation energy. Such behavior is well known for the D-line in CNTs but also for conjugated polymers like poly-acetylene.[42] It is an indication for defective structures where vibrational frequencies and electronic

Table 2: Transition energies in eV as observed experimentally from resonance Raman analysis, compared to calculated values (in parentheses) and to references for AGNR. Experimental values were rounded to two digits behind the decimal point. Line 1 and line 3 were obtained for 7-AGNR from high frequency modes and from the RBLM, respectively. Column 5 and 6 are from references. The table also shows calculated transition energies for 5-AGNR, together with a value from a reference.

Ribbon	E_{11} Exp. (Calc.) (eV)	E_{22} Exp. (Calc.) (eV)	E_{33} (eV)	E_{11} Exp. (Calc.) (eV)	E_{22} Exp. (Calc.) (eV)
7-AGNR	2.18	2.45		2.1 Ref. [8]	2.3 Ref. [8]
	(2.37)	(2.75)	(3.03)	(1.91)	(2.3)
7RBLM	2.18	2.43			
6-AGNR	1.83			1.69 Ref.[40]	
	(1.82)	(3.02)	(3.24)		
5-AGNR	(0.84)	(2.19)	(3.02)	0.1 Ref.[41]	

transitions exhibit some correlation which eventually leads to photo-selective resonance scattering. In our case such structures may be represented by interfaces between extended or short ribbons of different structure and different topology. In such cases new electronic state inside the gap can be created.[17] Also, modified edges resulting in sample inhomogeneity can lead to slightly modified RBLM-modes and thus result in photo-selective resonance scattering. In addition to the shoulder a very weak Raman signal is observed at 375 cm^{-1} for 506.1 nm excitation and at shorter wavelength of 460 nm a Raman line at 417 cm^{-1}. At even shorter wavelengths of 405 nm excitation a Raman line is observed at 533 cm^{-1}. (The latter two are not shown in the figure.) The origin of these lines will be discussed below and in some more detail in Supporting Informations Section (e).

The strong line at 414 cm^{-1} is most appropriate to analyze resonance profiles. This profile is depicted in the Fig. 4c. It exhibits two strong resonances and a weak resonance at 2.7 eV, which is not statistically significant and originates from a differentRaman frequency (see Supporting Information (e)). Due to the low mode energy for the RBLM(51 meV) the two resonances do not explicitly show vibronic splitting. Fitting the strong resonances with the Albrecht A term yields the transition energies listed in Tab. 2. The resonances have very similar energies as they were observed for the high frequency modes of the 7-AGNR and are therefore assigned to E_{11} and E_{22}.

RBLMs for AGNR are known to depend on the width w of the ribbons. In several reports this dependence was observed to follow an $1/\sqrt{w}$ behavior [20]. A more recent work showed that the RBLM was found to scale with 1/w.[21] Within the small frequency range one cannot discriminate

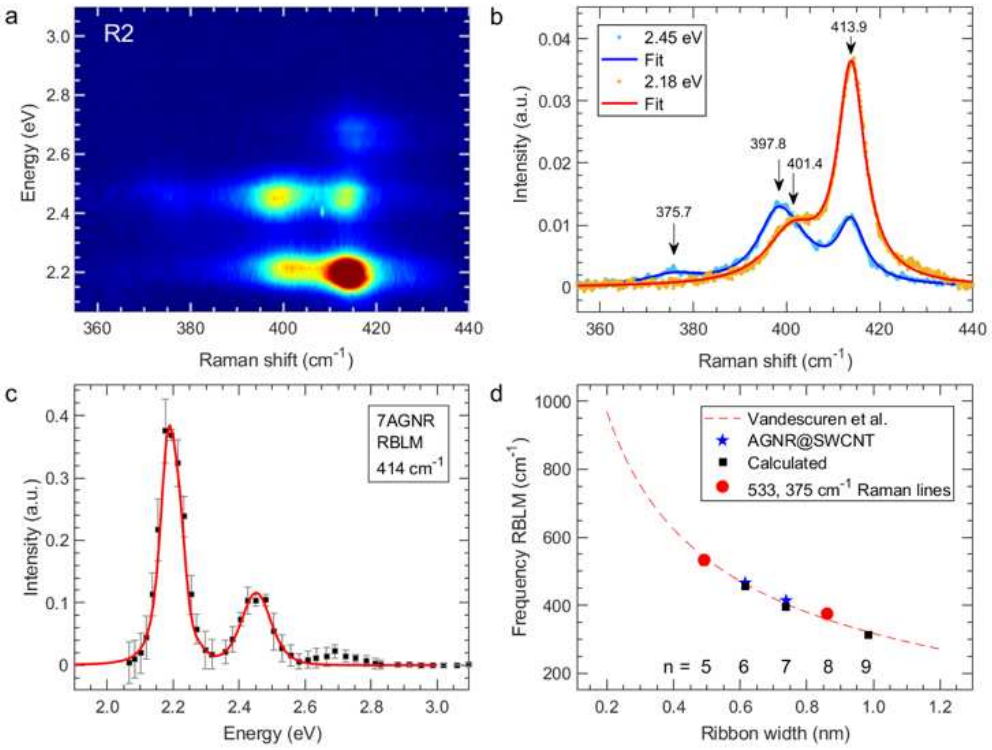

Figure 4: Raman scattering for the RBLM of 7-AGNR. a, Blown up Raman map for the frequency region between 350 and 440 cm^{-1}; b, Radial breathing like mode for 7-AGNR as excited with laser lines at 2,45 (blue) and 2,18 eV (red). Full drawn lines are fits from the experimental analysis. c, Resonance profile for the main peak of the RBLM at 414 cm^{-1} (dots, with errorbars) together with the calculated values (red line); d, RBLMs frequencies versus ribbon width w. Blue stars are the experimental results from this work. Black squares are calculated values. The dashed line corresponds to Vanderscuren et al.[20] who found a relation of the form $\omega_{\mathrm{RBLM}} = a/\sqrt{w} - b$ with empirical parameters a and b for the dependence of the RBLM frequency on w, the ribbon width without hydrogen. The dashed line in the figure was evaluated for a and b equal to 527.4 and 210.2, respectively. Red dots are for the additional Raman lines at 533 and 375 cm^{-1} if they are assigned to 5-AGNR and 8AGNR, respectively. The value for n = 9 is from a reference.[7]

between the two scaling laws. Figure 4d depicts this scaling law (Vandescuren diagram) as a dashed line. The black squares are the frequencies calculated here for 5-AGNR, 6-AGNR and 7-AGNR. The experimentally observed frequencies for 6-AGNR and 7-AGNR are indicated as blue stars. The good fit of these values into the Vandescuren diagram is another proof for the observation of such ribbons in our samples. Interestingly the so far unassigned lines at 533 cm^{-1} and 375 cm^{-1} fit also very well to the diagram if they are assigned to RBLMs for 5-AGNR and 8-AGNR. Recently the RBLM for 5-AGNR was observed at 533 cm^{-1}.[12,43] However, since both ribbons are narrow gap species of the type 3p+2, E_{22} resonances or even higher transitions must be involved for their observation. Interestingly for 8-AGNR very recently an effective gap of 2.3 eV was reported from STS measurements.[44] This is reasonably close to the 2.45 eV laser used to detect the Raman line at 375 cm^{-1}. The Raman line at 533 cm^{-1} was observed in our case for excitation with a considerable higher energy than the value calculated for the E_{22} transition. Shortening of the ribbons with respect to infinite long species could be the reason for the enhanced transition energies[41,45] as they are observed here.

4 Discussion and Conclusion

Discussion

When using polyaromatic hydrocarbons as precursor molecules (such as coronene[29,30]), the growth of GNRs inside CNTs can be explained by an oligomerization reaction. In our case, however, and similarly as previously reported for tetrathiofulvalene molecules inside CNTs,[28]

the encapsulated ferrocene molecules first need to be decomposed by the heat treatment and subsequently need to form the nanoribbons. This process is assumed to benefit from the graphene-like walls of the nanotubes, but the exact process is yet unknown. Until now, only graphene nanoribbons with armchair structures were observed, which is probably due to the higher stability of these ribbons. The dominance of the growth of 6AGNR and 7AGNR is due to the mean diameter of the carbon nanotubes used. Ribbons with a higher width would not fit into the tubes without extra stress and too narrow ribbons would would be energetically less favorable.

The ribbons observed in our study are definitely hydrogen passivated. This can be concluded from the strong CH-ipb mode observed in the Raman spectra. The strong response of the hydrogen vibration is also reflected in the ab initio calculations. Passivation by more extended hydrocarbon groups is not likely due to the lack of space inside the tubes.

The concentration of the ribbons inside the tubes can be estimated from the available carbon resources and thus the degree of filling of the tubes with ferrocene. A (17,0) tube can be filled with approximately 4 molecules of ferrocene per nm,[46] which means 40 C/nm can be provided. A 7-AGNR needs 33.3 C/nm, hence providing sufficient carbon atoms to form the graphene nanoribbons and thus a high concentration of ribbons can be expected. We indeed observe very high Raman intensities from the AGNRs compared to the Raman signatures of the surrounding CNTs, however, the Raman cross-section of encapsulated AGNRs with respect those of CNTs is not yet known. Hence, one cannot use the Raman intensities to estimate the synthesis yield.

The TEM analysis gives clear evidence for flat objects with ribbon structure inside the tubes.

The deviation from a perfect graphenic ribbon structure observed in the figure is a consequence of the electron beam irradiation rather than being intrinsic to the ribbon growth. The identification of the ribbons comes from wavelength-dependent Raman scattering and comparison to high level quantum-chemical calculations. The very narrow Raman lines as depicted in Tab. 1 and Fig. 2 are evidence for clean and highly unperturbed ribbon material. For the 7-AGNR the experimental and theoretical Raman spectra exhibit unprecedented agreement with respect to frequency of the modes and the relative Raman intensities.

The very sharp and individual peaks of the resonance profiles are evidence for a well-defined edge structure, which does not allow for defect induced modulation and consequently broadening or splitting of the optical transitions.

Conclusion

The results presented above demonstrate that graphene nanoribbons can be grown from thermal decomposition of ferrocene encapsulated in carbon nanotubes. Aberration corrected high resolution transmission electron microscopy provides evidence for the ribbons inside the tubes. Raman scattering combined with first principle calculations and resonance excitation analysis is an excellent tool to identify the structure of GNR even if the ribbons are encapsulated in SWCNTs. Due to its nondestructive nature and frequency selective character the Raman method is superior to any other optical method such as optical absorption or luminescence spectroscopy. In addition the method allows determining the electronic structures of the ribbons, even beyond the HOMO-LUMO gap. The results provide a challenge that ribbons with larger or smaller width than those

reported here, can be grown in larger or smaller SWCNTs, respectively, and can be detected with Raman scattering. They thus open a new field in subnanometer graphene ribbon research.

5 Methods

Synthesis of GNRs@SWCNT SWCNTs as grown by the eDIPS technique [47] with mean diameter around 1.3 nm were used as a starting material. All tubes were purified by first etching in air and subsequent treating with HCl as described previously [48] to remove amorphous carbon and catalytic particles from tube growth. SWCNT bucky paper was obtained by washing and filtering the tubes with distilled water and ethanol.

For the filling process the tubes were first opened by etching in air at 420 °C and then exposed to ferrocene at 400 °C for two days in previously evacuated quartz tubes. The transformation of the $FeCp_2$ molecules to the AGNRs inside the tubes was performed by vacuum annealing for several days and at various temperatures as described in the main text. This process resulted in the appearance of new lines in the Raman spectra from some so far unknown objects. Control experiments were performed without opening the tubes but otherwise treating the material identically. In this case almost no new Raman lines were observed as depicted explicitly in the Supporting Information Section (c). This can be considered as evidence for the growth of the objects inside the tubes.

Analysis by Transmission Electron Microscopy To obtain information on the grown objects TEM investigations were performed with a Thermo Fisher (formerly FEI) TITAN G2 80-

300 (Fig. 1a-e) at 80 kV. Figure 1f, g and i are acquired by the specific Thermo Fisher (formerly FEI) SALVE (subangstrom low voltage electron microscopy) transmission electron microscope fitted with a CEOS CETCOR spherical aberration corrector (axial 5th order, off-axial 3rd order), a chromatic aberration corrector, and a Thermo Fisher Ceta 4K CMOS camera. The exposure time of the images is 1.0 s and the dose rate is 6.85*10^6 electrons s^{-1} nm^{-2}.

Theoretical evaluation vibrational frequencies and mode-specific Raman intensities Vibrational frequencies of the ribbons were calculated at the Γ point using the Vienna Ab initio Simulation Package (VASP).[49] Raman intensities I_s were evaluated using the frequency dependent Placzek approximation. In this case the intensity of the Raman lines is proportional to the square of the derivative of the frequency dependent polarizability with respect to the phonon normal mode:

$$I_s(\omega_s, \omega_L) = \frac{\omega_s^4}{\omega_L} \sum_{\rho,\sigma} \left| \frac{\partial \alpha_{\rho,\sigma}(\omega_L)}{\partial Q_{ph}} \right|^2 \Gamma(\omega - \omega_{ph})(n(\omega_{ph}) + 1) \quad (3)$$

where $\alpha_{\rho,\sigma}(\omega_L)$ is the dynamic (frequency dependent) polarizability tensor evaluated from first principle calculations at the laser energy ω_L. Calculation of the dynamic polarizability was done within the linear response theory [50] with wave functions and structural parameters used during the frequency calculation and geometrical optimization. Q_{ph} and ω_{ph} are the phonon normal modes and frequencies, respectively, and ω_s is the frequency of the scattered light. ω is the difference between ω_L and ω_s. $n(\omega_{ph})$ is the Bose-Einstein distribution at room temperature and $\Gamma(x)$ is a normalized Lorentzian function with full width at half maximum of 10 cm^{-1}. Numeric derivatives of the polarizability tensor were calculated using symmetric derivatives by manually shifting the atoms according to normal modes in both positive and negative directions. From this the following

expression can be obtained for the derivative of the polarizability:

$$\frac{\partial \alpha_{\rho,\sigma}(\omega_L)}{\partial Q_{ph}} = \sum_{r,s} \frac{\langle f|H_{e-p}|s\rangle\langle s|H_{e-ph}|r\rangle\langle r|H_{e-p}|i\rangle}{(\omega_L - \omega_r - \mathrm{i}\gamma_{e-p})(\omega_r - \omega_s - \mathrm{i}\gamma_{e-ph})} \tag{4}$$

where r,s are intermediate virtual electronic states with energy $\omega_{r,s}$ obtained from first principle calculations, H_{e-ph} (derivative of the electron-ion potential with respect to the normal modes) and H_{e-p} are the Hamiltonians for the electron-phonon and electron-photon coupling, respectively and γ_{e-ph} and γ_{e-p} are the corresponding damping constants (life times). Details of the derivation can be found in ref. [32]. The calculation was successfully used previously for the analysis of doping and strain induced changes of the Raman spectra and gap structure of MoS_2 [51] and silicene.[52]

Optical excitation energies were calculated by solving the Bethe-Salpeter equation within the frame of a quasiparticle self-consistent GW calculation as built in the QUESTAAL code [53] with ladder diagram corrections. [54] Excitation energies were determined by taking the energy values at the maximum of the peaks present in the imaginary part of the macroscopic dielectric function. Explicitly, calculations were performed for the low gap 3p+2 ribbon 5-AGNR, for the moderate gap 3p ribbon 6-AGNR, and for the large gap 3p+1 ribbon 7-AGNR. More details on the calculation are in supporting Information Section (b).

Raman scattering Raman spectra were excited at room temperature and at ambient conditions with various lasers in the visible spectral range. Spectra were recorded with a Dilor xy800 and with a Labram HR800 microscope. In Figure 2 spectra with a spectral resolution of less than 2 wavenumbers. Thus the observed linewidths are intrinsic to the ribbon material. Raman intensities were normalized to the 2D line of the carbon nanotubes, since the 2D-line is known to

be highly independent from defects. In the case of resonance analysis normalization was performed to the fundamental Raman line of Si.

Evaluation of Excitation Profile Resonance Raman spectra were evaluated for wavelength dependent excitation in the range between 400 and 800 nm with 5 nm step-size. To cover the requested energy range for excitation the following three laser systems were used. 400-526 nm: A frequency-doubled Ti:Sa laser (Msquared SolsTis external cavity frequency doubled ECD-X module) which was pumped by an 18 W Sprout-G diode pumped solid state laser (532 nm). 534-605nm and 610-690 nm: A dye laser (spectra Physics model 375) pumped by an Ar+ ion laser (Spectra physics 2020) equipped with either Rhodamine 110 or DCM laser dyes. 690-800 nm: A tunable Ti:Sa laser (Spectra Physics 3900S). The Raman spectra were recorded with a high resolution triple grating Dilor XY800 spectrometer and a liquid nitrogen cooled CCD detector. More details about the recording and evaluation of the Raman spectra can be obtained from Supporting Information Section (e).

6 Acknowledgement

Work supported by the NSFC (51902353), the FWF project P21333-N20, and the NKFIH, Grant No. K-115608. L.S. acknowledges the financial support from the Natural Science Foundation of Guangdong Province (Grant No. 2019A1515011227) and the Sun Yat-Sen University (Grant No. 29000-18841218, 29000-31610028) J.K., J.K. and G.K. further acknowledge the [NIIF] for awarding access to resource based in Hungary at Debrecen, they further acknowledge support

by the National Research Development and Innovation Office of Hungary within the Quantum Technology National Excellence Program (Project No. 2017-1.2.1-NKP-2017-00001), and the ELTE Excellence Program (1783-3/2018/FEKUTSTRAT) supported by the Hungarian Ministry of Human Capacities. K.C. acknowledges the China Scholarship Council (CSC) for financial support. U.K. acknowledges the support of the Graphene Flagship and DFG SPP Graphene as well as the DFG and the Ministry of Science, Research and the Arts (MWK) of Baden-Wuerttemberg within the frame of the SALVE project. M.M., S.C., and W.W. acknowledge funding from the Fund for Scientific Research Flanders (FWO projects No. G040011N, G02112N, G035918N, G036618N and the EOS-charming project G0F6218N [EOS-ID 30467715]). M.M. acknowledges funding of a DOCPRO4 PhD scholarship from the UAntwerp research fund (BOF) and S.C. also acknowledges funding from the European Research Council Starting Grant No. 679841.

7 Author Contributions

H.K. and L.S. contributed equally to this work. H.K. and L.S. designed and supervised the experiments. L.S. prepared the samples and did the characterization with spontaneous Raman scattering in Vienna with lasers at wavelength of 633 and 568 nm. S.C., M.M., and W.W. performed the wavelength-dependent resonance Raman scattering experiments and their analysis. H.K. analyzed the resonance profiles. K.C. and U.K. performed HRTEM characterization and simulations. J.K., J.K., and G.K. performed the first principles DFT calculations. T.S. provided the SWCNTs. T.P. provided the laboratory facilities and the Raman setup in Vienna. All authors discussed the results and commented on the manuscript at all stages.

8 Competing Financial Interests

The authors declare that they have no competing financial interests associated to the publication of this manuscript.

Corresponding Author hans.kuzmany@univie.ac.at, shilei26@mail.sysu.edu.cn

References

1. Bennett, P. B. et al. Bottom-up graphene nanoribbon field-effect transistors. Appl. Phys. Lett. **103**, 253114 (2013).

2. Martini, L. Graphene nanoribbon devices. Carbon **146**, 36–42 (2019).

3. Novoselov, K. S. et al. Electric field effect in atomically thin carbon films. Science **306**, 666–669 (2004).

4. Son, Y. W., Cohen, M. L. & Louie, S. G. Energy gaps in graphene nanoribbons. Phys. Rev. Lett. **97**, 216803 (2006).

5. Barone, V., Hod, O. & Scuseria, G. E. Electronic structure and stability of semiconducting graphene nanoribbons. Nano Lett. **6**, 2748–2754 (2006).

6. Cai, J. et al. Atomically precise bottom-up fabrication of graphene nanoribbons. Nature **466**, 470–473 (2010).

7. Talirz, L., Ruffieux, P. & Fasel, R. On-surface synthesis of atomically precise graphene nanoribbons. Adv. Mater. **28**, 6222–6231 (2016).

8. Denk, R. et al. Exciton-dominated optical response of ultra-narrow graphene nanoribbons. Nat. Commun. **5**, 4253 (2014).

9. Durr, R. A. et al. Orbitally matched edge-doping in graphene nanoribbons. J. Am. Chem. Soc. **140**, 807–813 (2018).

10. Sun, Q. et al. Massive dirac fermion behavior in a low bandgapgraphene nanoribbon near a topological phase boundary. Adv. Mater. **32**, 1906054 (2020).

11. Gigli, L. et al. Detachment dynamics of graphene nanoribbons on gold. ACS Nano **13**, 689–697 (2019).

12. Overbeck, J. et al. Optimized substrates and measurement approaches for Raman spectroscopy of graphene nanoribbons. Phys. Stat. Sol. B 1900343 (2019).

13. Verbitskiy, I. A. et al. Raman fingerprints of atomically precise graphene nanoribbons. Nano Lett. **16**, 3442–3447 (2016).

14. Pedramrazi, Z. et al. Concentration dependence of dopant electronic structure in bottom-up graphene nanoribbons. Nano Lett. **18**, 3550–3556 (2018).

15. Narita, A., Chen, Z. P., Chen, Q. & Mullen, K. Solution and on-surface synthesis of structurally defined graphene nanoribbons as a new family of semiconductors. Chemical Science **10**, 964–975 (2019).

16. Chen, Y. C. et al. Molecular bandgap engineering of bottom-up synthesized graphene nanoribbon heterojunctions. Nat. Nanotechnol. **10**, 156–160 (2015).

17. Cao, T., Zhao, F. & Louie, S. G. Topological phases in graphene nanoribbons: junction states, spin centers, and quantum spin chains. Phys. Rev. Lett. **119**, 076401 (2017).

18. Groning, O. et al. Engineering of robust topological quantum phases in graphene nanoribbons. Nature **560**, 209–213 (2018).

19. Akilimali, R. et al. Graphene nanoribbon-tio2-quantum dots hybrid photoanode to boost the performance of photoelectrochemical for hydrogen generation. Catal. Today **340**, 161–169 (2020).

20. Vandescuren, M., Hermet, P., Meunier, V., Henrard, L. & Lambin, P. Theoretical study of the vibrational edge modes in graphene nanoribbons. Phys. Rev. B **78**, 195401 (2008).

21. Liu, D., Daniels, C., Meunier, V., Every, A. G. & Tománek, D. In-plane breathing and shear modes in low-dimensional nanostructures. Carbon **157**, 364–370 (2020).

22. Lim, H. E. et al. Growth of carbon nanotubes via twisted graphene nanoribbons. Nature Comm. **4**, 2548 (2013).

23. Khlobystov, A. N. Carbon nanotubes: From nano test tube to nano-reactor. ACS Nano **5**, 9306–9312 (2011).

24. Kuzmany, H. et al. The growth of new extended carbon nanophases from ferrocene inside single-walled carbon nanotubes. Phys. Stat. Sol. RRL **11**, 1700158 (2017).

25. Kitaura, R. et al. High-yield synthesis of ultrathin metal nanowires in carbon nanotubes. Angew. Chem. Int. Ed. **48**, 8298–8302 (2009).

26. Shi, L. et al. Confined linear carbon chains as a route to bulk carbyne. Nature Mater. **15**, 634–639 (2016).

27. Pham, T. et al. Torsional instability in the single-chain limit of a transition metal trichalcogenide. Science **361**, 263–266 (2018).

28. Chamberlain, T. W. et al. Size, structure, and helical twist of graphene nanoribbons controlled by confinement in carbon nanotubes. ACS Nano **6**, 3943–3953 (2012).

29. Chernov, A. I. et al. Optical properties of graphene nanoribbons encapsulated in single-walled carbon nanotubes. ACS Nano **7**, 6346–6353 (2013).

30. Anoshkin, I. V. et al. Coronene encapsulation in single-walled carbon nanotubes: Stacked columns, peapods, and nanoribbons. Chemphyschem **15**, 1660–1665 (2014).

31. Lim, H. E. et al. Fabrication and optical probing of highly extended, ultrathin graphene nanoribbons in carbon nanotubes. ACS Nano **9**, 5034–5040 (2015).

32. Kukucska, G., Zólyomi, V. & Koltai, J. Frequency-dependent ab initio resonance raman spectroscopy. arXiv preprint arXiv:1903.00253 (2019).

33. Chuvilin, A. et al. Self-assembly of a sulphur-terminated graphene nanoribbon within a single-walled carbon nanotube. Nat. Mater. **10**, 687–692 (2011).

34. Kuzmany, H., Shi, L. & Pichler, T. The origin of nondispersive raman lines in the d-band region for ferrocene@hipco swcnts transformed at high temperatures. Phys. Stat. Sol. B **252**, 2530 – 2535 (2015).

35. Borin Barin, G. et al. Substrate transfer and ex situ characterization of on-surface synthesized graphene nanoribbons. ACS Appl. Nano Mater. **2**, 2184–2192 (2019).

36. Basagni, A. et al. Molecules-oligomers-nanowires-graphene nanoribbons: A bottom-up stepwise on-surface covalent synthesis preserving long-range order. J. Am. Chem. Soc. **137**, 1802–1808 (2015).

37. Kiefer, W. Nonlinear raman spectroscopy infrared and raman spectroscopy ed b schrader (1995).

38. Haroz, E. H. et al. Resonant Raman spectroscopy of armchair carbon nanotubes: Absence of broad G- feature. Phys. Rev. B **84**, 121403 (2011).

39. Tang, J. & Albrecht, A. Developments in the theories of vibrational raman intensities. In Raman Spectroscopy, 33–68 (Springer, 1970).

40. Merino-Diez, N. et al. Width-dependent band gap in armchair graphene nanoribbons reveals fermi level pinning on Au(111). ACS Nano **11**, 11661–11668 (2017).

41. Kimouche, A. et al. Ultra-narrow metallic armchair graphene nanoribbons. Nat. Commun. **6**, 10177 (2015).

42. Kuzmany, H., Imhoff, E. A., Fitchen, D. B. & Sarhangi, A. Frank-condon approach for optical-absorption and resonance Raman-scattering in trans-polyacetylene. Phys. Rev. B **26**, 7109–7112 (1982).

43. Chen, Z. P. et al. Lateral fusion of chemical vapor deposited N=5 armchair graphene nanoribbons. J. Am. Chem. Soc. **139**, 9483–9486 (2017).

44. Sun, K. & Ji, P. On-surface synthesis of 8- and 10-armchair graphene nanoribbons. Small **15**, 1804526 (2019).

45. Talirz, L., Sde, H. & Kawai, S. Band gap of atomically precise graphene nanoribbons as a function of ribbon length and termination. Chem. Phys. Chem. **20**, 2348–2353 (2019).

46. Plank, W. et al. Electronic structure of carbon nanotubes with ultrahigh curvature. ACS Nano **4**, 4515–4522 (2010).

47. Saito, T. et al. Selective diameter control of single-walled carbon nanotubes in the gas-phase synthesis. J. Nanosci. Nanotechn. **8**, 6153–6157 (2008).

48. Kuzmany, H. et al. Nondispersive raman lines in the d-band region for ferrocene functionalized carbon nanotubes. Phys. Stat. Sol. B **251**, 2457 – 2460 (2014).

49. Kresse, G. & Furthmuller, J. Efficient iterative schemes for ab-initio total-energy calculations using a plane-wave basis set. Phys. Rev. B **54**, 11169–11186 (1996).

50. Gajdos, M., Hummer, K., Kresse, G., Furthmuller, J. & Bechstedt, F. Linear optical properties in the projector-augmented wave methodology. Phys. Rev. B **73**, 045112 (2006).

51. Pető, J. et al. Moderate strain induced indirect bandgap and conduction electrons in mos 2 single layers. npj 2D Mater. Appl. **3**, 1–6 (2019).

52. Kukucska, G., Zolyomi, V. & Koltai, J. Characterization of epitaxial silicene with Raman spectroscopy. Phys. Rev. B **98**, 075437 (2018).

53. Kotani, T. & van Schilfgaarde, M. Quasiparticle self-consistent gw method: A basis for the independent-particle approximation. Phys. Rev. B **76**, 165106 (2007).

54. Cunningham, B., Gruning, M., Azarhoosh, P., Pashov, D. & van Schilfgaarde, M. Effect of ladder diagrams on optical absorption spectra in a quasiparticle self-consistent gw framework. Phys. Rev. Materials **2**, 034603 (2018).